



Measurement of the $e^+e^- \rightarrow \Sigma^0 \bar{\Sigma}^0$ cross sections at center-of-mass energies from 2.3864 to 3.0200 GeV



BESIII Collaboration

M. Ablikim^a, M.N. Achasov^{j,4}, P. Adlarson^{bs}, S. Ahmed^o, M. Albrecht^d, A. Amoroso^{bp,br}, Q. An^{bm,ax}, Y. Bai^{aw}, O. Bakina^{ae}, R. Baldini Ferroli^w, I. Balossino^y, Y. Ban^{an,12}, K. Begzsuren^{ab}, J.V. Bennett^e, N. Berger^{ad}, M. Bertani^w, D. Bettoni^y, F. Bianchi^{bp,br}, J. Biernat^{bs}, J. Bloms^{bj}, A. Bortone^{bp,br}, I. Boyko^{ae}, R.A. Briere^e, H. Cai^{bt}, X. Cai^{a,ax}, A. Calcaterra^w, G.F. Cao^{a,be}, N. Cao^{a,be}, S.A. Cetin^{bb}, J.F. Chang^{a,ax}, W.L. Chang^{a,be}, G. Chelkov^{ae,2,3}, D.Y. Chen^f, G. Chen^a, H.S. Chen^{a,be}, M.L. Chen^{a,ax}, S.J. Chen^{al}, X.R. Chen^{aa}, Y.B. Chen^{a,ax}, W. Cheng^{br}, G. Cibinetto^y, F. Cossio^{br}, X.F. Cui^{am}, H.L. Dai^{a,ax}, J.P. Dai^{ar,8}, X.C. Dai^{a,be}, A. Dbeyssi^o, R.B. de Boer^d, D. Dedovich^{ae}, Z.Y. Deng^a, A. Denig^{ad}, I. Denysenko^{ae}, M. Destefanis^{bp,br}, F. De Mori^{bp,br}, Y. Ding^{aj}, C. Dong^{am}, J. Dong^{a,ax}, L.Y. Dong^{a,be}, M.Y. Dong^{a,ax,be}, S.X. Du^{bw}, J. Fang^{a,ax}, S.S. Fang^{a,be}, Y. Fang^a, R. Farinelli^{y,z}, L. Fava^{bq,br}, F. Feldbauer^d, G. Felici^w, C.Q. Feng^{bm,ax}, M. Fritsch^d, C.D. Fu^a, Y. Fu^a, X.L. Gao^{bm,ax}, Y. Gao^{bn}, Y. Gao^{an,12}, Y.G. Gao^f, I. Garzia^{y,z}, E.M. Gersabeck^{bh}, A. Gilman^{bi}, K. Goetzen^k, L. Gong^{am}, W.X. Gong^{a,ax}, W. Gradl^{ad}, M. Greco^{bp,br}, L.M. Gu^{al}, M.H. Gu^{a,ax}, S. Gu^b, Y.T. Gu^m, C.Y. Guan^{a,be}, A.Q. Guo^v, L.B. Guo^{ak}, R.P. Guo^{ap}, Y.P. Guo^{ad}, Y.P. Guo^{i,9}, A. Guskov^{ae}, S. Han^{bt}, T.T. Han^{aq}, T.Z. Han^{i,9}, X.Q. Hao^p, F.A. Harris^{bf}, K.L. He^{a,be}, F.H. Heinsius^d, T. Held^d, Y.K. Heng^{a,ax,be}, M. Himmelreich^{k,7}, T. Holtmann^d, Y.R. Hou^{be}, Z.L. Hou^a, H.M. Hu^{a,be}, J.F. Hu^{ar,8}, T. Hu^{a,ax,be}, Y. Hu^a, G.S. Huang^{bm,ax}, L.Q. Huang^{bn}, X.T. Huang^{aq}, Z. Huang^{an,12}, N. Huesken^{bj}, T. Hussain^{bo}, W. Ikegami Andersson^{bs}, W. Imoehl^v, M. Irshad^{bm,ax}, S. Jaeger^d, S. Janchiv^{ab,11}, Q. Ji^a, Q.P. Ji^p, X.B. Ji^{a,be}, X.L. Ji^{a,ax}, H.B. Jiang^{aq}, X.S. Jiang^{a,ax,be}, X.Y. Jiang^{am}, J.B. Jiao^{aq}, Z. Jiao^r, S. Jin^{al}, Y. Jin^{bg}, T. Johansson^{bs}, N. Kalantar-Nayestanaki^{ag}, X.S. Kang^{aj}, R. Kappert^{ag}, M. Kavatsyuk^{ag}, B.C. Ke^{as,a}, I.K. Keshk^d, A. Khoukaz^{bj}, P. Kiese^{ad}, R. Kiuchi^a, R. Kliemt^k, L. Koch^{af}, O.B. Kolcu^{bb,6}, B. Kopf^d, M. Kuemmel^d, M. Kuessner^d, A. Kupsc^{bs}, M.G. Kurth^{a,be}, W. Kühn^{af}, J.J. Lane^{bh}, J.S. Lange^{af}, P. Larin^o, L. Lavezzi^{br}, H. Leithoff^{ad},

* E-mail address: besiii-publications@ihep.ac.cn.

¹ Also at Bogazici University, 34342 Istanbul, Turkey.

² Also at the Moscow Institute of Physics and Technology, Moscow 141700, Russia.

³ Also at the Functional Electronics Laboratory, Tomsk State University, Tomsk, 634050, Russia.

⁴ Also at the Novosibirsk State University, Novosibirsk, 630090, Russia.

⁵ Also at the NRC "Kurchatov Institute", PNPI, 188300, Gatchina, Russia.

⁶ Also at Istanbul Arel University, 34295 Istanbul, Turkey.

⁷ Also at Goethe University Frankfurt, 60323 Frankfurt am Main, Germany.

⁸ Also at Key Laboratory for Particle Physics, Astrophysics and Cosmology, Ministry of Education; Shanghai Key Laboratory for Particle Physics and Cosmology; Institute of Nuclear and Particle Physics, Shanghai 200240, People's Republic of China.

⁹ Also at Key Laboratory of Nuclear Physics and Ion-beam Application (MOE) and Institute of Modern Physics, Fudan University, Shanghai 200443, People's Republic of China.

¹⁰ Also at Harvard University, Department of Physics, Cambridge, MA, 02138, USA.

¹¹ Currently at: Institute of Physics and Technology, Peace Ave.54B, Ulaanbaatar 13330, Mongolia.

¹² Also at State Key Laboratory of Nuclear Physics and Technology, Peking University, Beijing 100871, People's Republic of China.

¹³ School of Physics and Electronics, Hunan University, Changsha 410082, China.

M. Lellmann^{ad}, T. Lenz^{ad}, C. Li^{ao}, C.H. Li^{ai}, Cheng Li^{bm,ax}, D.M. Li^{bw}, F. Li^{a,ax}, G. Li^a, H.B. Li^{a,be}, H.J. Li^{i,9}, J.L. Li^{aq}, J.Q. Li^d, Ke Li^a, L.K. Li^a, Lei Li^c, P.L. Li^{bm,ax}, P.R. Li^{ah}, S.Y. Li^{az}, W.D. Li^{a,be}, W.G. Li^a, X.H. Li^{bm,ax}, X.L. Li^{aq}, Z.B. Li^{ay}, Z.Y. Li^{ay}, H. Liang^{bm,ax}, H. Liang^{a,be}, Y.F. Liang^{au}, Y.T. Liang^{aa}, L.Z. Liao^{a,be}, J. Libby^u, C.X. Lin^{ay}, B. Liu^{ar,8}, B.J. Liu^a, C.X. Liu^a, D. Liu^{bm,ax}, D.Y. Liu^{ar,8}, F.H. Liu^{at}, Fang Liu^a, Feng Liu^f, H.B. Liu^m, H.M. Liu^{a,be}, Huanhuan Liu^a, Huihui Liu^q, J.B. Liu^{bm,ax}, J.Y. Liu^{a,be}, K. Liu^a, K.Y. Liu^{aj}, Ke Liu^f, L. Liu^{bm,ax}, Q. Liu^{be}, S.B. Liu^{bm,ax}, Shuai Liu^{av}, T. Liu^{a,be}, X. Liu^{ah}, Y.B. Liu^{am}, Z.A. Liu^{a,ax,be}, Z.Q. Liu^{aq}, Y.F. Long^{an,12}, X.C. Lou^{a,ax,be}, F.X. Lu^p, H.J. Lu^r, J.D. Lu^{a,be}, J.G. Lu^{a,ax}, X.L. Lu^a, Y. Lu^a, Y.P. Lu^{a,ax}, C.L. Luo^{ak}, M.X. Luo^{bv}, P.W. Luo^{ay}, T. Luo^{i,9}, X.L. Luo^{a,ax}, S. Lusso^{br}, X.R. Lyu^{be}, F.C. Ma^{aj}, H.L. Ma^a, L.L. Ma^{aq}, M.M. Ma^{a,be}, Q.M. Ma^a, R.Q. Ma^{a,be}, R.T. Ma^{be}, X.N. Ma^{am}, X.X. Ma^{a,be}, X.Y. Ma^{a,ax}, Y.M. Ma^{aq}, F.E. Maas^o, M. Maggiora^{bp,br}, S. Maldaner^{ad}, S. Malde^{bk}, Q.A. Malik^{bo}, A. Mangoni^x, Y.J. Mao^{an,12}, Z.P. Mao^a, S. Marcello^{bp,br}, Z.X. Meng^{bg}, J.G. Messchendorp^{ag}, G. Mezzadri^y, T.J. Min^{al}, R.E. Mitchell^v, X.H. Mo^{a,ax,be}, Y.J. Mo^f, N.Yu. Muchnoi^{j,4}, H. Muramatsu^{bi}, S. Nakhoul^{k,7}, Y. Nefedov^{ae}, F. Nerling^{k,7}, I.B. Nikolaev^{j,4}, Z. Ning^{a,ax}, S. Nisar^{h,10}, S.L. Olsen^{be}, Q. Ouyang^{a,ax,be}, S. Pacetti^x, X. Pan^{av}, Y. Pan^{bh}, A. Pathak^a, P. Patteri^w, M. Pelizaeus^d, H.P. Peng^{bm,ax}, K. Peters^{k,7}, J. Pettersson^{bs}, J.L. Ping^{ak}, R.G. Ping^{a,be}, A. Pitka^d, R. Poling^{bi}, V. Prasad^{bm,ax}, H. Qi^{bm,ax}, H.R. Qi^{az}, M. Qi^{al}, T.Y. Qi^b, S. Qian^{a,ax}, W.-B. Qian^{be}, Z. Qian^{ay}, C.F. Qiao^{be}, L.Q. Qin^l, X.P. Qin^m, X.S. Qin^d, Z.H. Qin^{a,ax}, J.F. Qiu^a, S.Q. Qu^{am}, K.H. Rashid^{bo}, K. Ravindran^u, C.F. Redmer^{ad}, A. Rivetti^{br}, V. Rodin^{ag}, M. Rolo^{br}, G. Rong^{a,be}, Ch. Rosner^o, M. Rump^{bj}, A. Sarantsev^{ae,5}, M. Savrié^z, Y. Schelhaas^{ad}, C. Schnier^d, K. Schoenning^{bs}, D.C. Shan^{av}, W. Shan^s, X.Y. Shan^{bm,ax}, M. Shao^{bm,ax}, C.P. Shen^b, P.X. Shen^{am}, X.Y. Shen^{a,be}, H.C. Shi^{bm,ax}, R.S. Shi^{a,be}, X. Shi^{a,ax}, X.D. Shi^{bm,ax}, J.J. Song^{aq}, Q.Q. Song^{bm,ax}, W.M. Song^{ac}, Y.X. Song^{an,12}, S. Sosio^{bp,br}, S. Spataro^{bp,br}, F.F. Sui^{aq}, G.X. Sun^a, J.F. Sun^p, L. Sun^{bt}, S.S. Sun^{a,be}, T. Sun^{a,be}, W.Y. Sun^{ak}, Y.J. Sun^{bm,ax}, Y.K. Sun^{bm,ax}, Y.Z. Sun^a, Z.T. Sun^a, Y.H. Tan^{bt}, Y.X. Tan^{bm,ax}, C.J. Tang^{au}, G.Y. Tang^a, J. Tang^{ay}, V. Thoren^{bs}, B. Tsednee^{ab}, I. Uman^{bd}, B. Wang^a, B.L. Wang^{be}, C.W. Wang^{al}, D.Y. Wang^{an,12}, H.P. Wang^{a,be}, K. Wang^{a,ax}, L.L. Wang^a, M. Wang^{aq}, M.Z. Wang^{an,12}, Meng Wang^{a,be}, W.H. Wang^{bt}, W.P. Wang^{bm,ax}, X. Wang^{an,12}, X.F. Wang^{ah}, X.L. Wang^{i,9}, Y. Wang^{bm,ax}, Y. Wang^{ay}, Y.D. Wang^o, Y.F. Wang^{a,ax,be}, Y.Q. Wang^a, Z. Wang^{a,ax}, Z.Y. Wang^a, Ziyi Wang^{be}, Zongyuan Wang^{a,be}, T. Weber^d, D.H. Wei^l, P. Weidenkaff^{ad}, F. Weidner^{bj}, S.P. Wen^a, D.J. White^{bh}, U. Wiedner^d, G. Wilkinson^{bk}, M. Wolke^{bs}, L. Wollenberg^d, J.F. Wu^{a,be}, L.H. Wu^a, L.J. Wu^{a,be}, X. Wu^{i,9}, Z. Wu^{a,ax}, L. Xia^{bm,ax}, H. Xiao^{i,9}, S.Y. Xiao^a, Y.J. Xiao^{a,be}, Z.J. Xiao^{ak}, X.H. Xie^{an,12}, Y.G. Xie^{a,ax}, Y.H. Xie^f, T.Y. Xing^{a,be}, X.A. Xiong^{a,be}, G.F. Xu^a, J.J. Xu^{al}, Q.J. Xuⁿ, W. Xu^{a,be}, X.P. Xu^{av}, L. Yan^{i,9}, L. Yan^{bp,br}, W.B. Yan^{bm,ax}, W.C. Yan^{bw}, Xu Yan^{av}, H.J. Yang^{ar,8}, H.X. Yang^a, L. Yang^{bt}, R.X. Yang^{bm,ax}, S.L. Yang^{a,be}, Y.H. Yang^{al}, Y.X. Yang^l, Yifan Yang^{a,be}, Zhi Yang^{aa}, M. Ye^{a,ax}, M.H. Ye^g, J.H. Yin^a, Z.Y. You^{ay}, B.X. Yu^{a,ax,be}, C.X. Yu^{am}, G. Yu^{a,be}, J.S. Yu^{t,13}, T. Yu^{bn}, C.Z. Yuan^{a,be}, W. Yuan^{bp,br}, X.Q. Yuan^{an,12}, Y. Yuan^a, Z.Y. Yuan^{ay}, C.X. Yue^{ai}, A. Yuncu^{bb,1}, A.A. Zafar^{bo}, Y. Zeng^{t,13}, B.X. Zhang^a, Guangyi Zhang^p, H.H. Zhang^{ay}, H.Y. Zhang^{a,ax}, J.L. Zhang^{bu}, J.Q. Zhang^d, J.W. Zhang^{a,ax,be}, J.Y. Zhang^a, J.Z. Zhang^{a,be}, Jianyu Zhang^{a,be}, Jiawei Zhang^{a,be}, L. Zhang^a, Lei Zhang^{al}, S. Zhang^{ay}, S.F. Zhang^{al}, T.J. Zhang^{ar,8}, X.Y. Zhang^{aq}, Y. Zhang^{bk}, Y.H. Zhang^{a,ax}, Y.T. Zhang^{bm,ax}, Yan Zhang^{bm,ax}, Yao Zhang^a, Yi Zhang^{i,9}, Z.H. Zhang^f, Z.Y. Zhang^{bt}, G. Zhao^a, J. Zhao^{ai}, J.Y. Zhao^{a,be}, J.Z. Zhao^{a,ax}, Lei Zhao^{bm,ax}, Ling Zhao^a, M.G. Zhao^{am}, Q. Zhao^a, S.J. Zhao^{bw}, Y.B. Zhao^{a,ax}, Y.X. Zhao^{aa}, Z.G. Zhao^{bm,ax}, A. Zhemchugov^{ae,2}, B. Zheng^{bn}, J.P. Zheng^{a,ax}, Y. Zheng^{an,12}, Y.H. Zheng^{be}, B. Zhong^{ak}, C. Zhong^{bn}, L.P. Zhou^{a,be}, Q. Zhou^{a,be}, X. Zhou^{bt}, X.K. Zhou^{be}, X.R. Zhou^{bm,ax}, A.N. Zhu^{a,be}, J. Zhu^{am}, K. Zhu^a, K.J. Zhu^{a,ax,be}, S.H. Zhu^{bl}, W.J. Zhu^{am}, X.L. Zhu^{az}, Y.C. Zhu^{bm,ax}, Z.A. Zhu^{a,be}, B.S. Zou^a, J.H. Zou^a

^a Institute of High Energy Physics, Beijing 100049, People's Republic of China^b Beihang University, Beijing 100191, People's Republic of China^c Beijing Institute of Petrochemical Technology, Beijing 102617, People's Republic of China^d Bochum Ruhr-University, D-44780 Bochum, Germany

- ^e Carnegie Mellon University, Pittsburgh, PA 15213, USA
^f Central China Normal University, Wuhan 430079, People's Republic of China
^g China Center of Advanced Science and Technology, Beijing 100190, People's Republic of China
^h COMSATS University Islamabad, Lahore Campus, Defence Road, Off Raiwind Road, 54000 Lahore, Pakistan
ⁱ Fudan University, Shanghai 200443, People's Republic of China
^j G.I. Budker Institute of Nuclear Physics SB RAS (BINP), Novosibirsk 630090, Russia
^k GSI Helmholtzcentre for Heavy Ion Research GmbH, D-64291 Darmstadt, Germany
^l Guangxi Normal University, Guilin 541004, People's Republic of China
^m Guangxi University, Nanning 530004, People's Republic of China
ⁿ Hangzhou Normal University, Hangzhou 310036, People's Republic of China
^o Helmholtz Institute Mainz, Johann-Joachim-Becher-Weg 45, D-55099 Mainz, Germany
^p Henan Normal University, Xinxiang 453007, People's Republic of China
^q Henan University of Science and Technology, Luoyang 471003, People's Republic of China
^r Huangshan College, Huangshan 245000, People's Republic of China
^s Hunan Normal University, Changsha 410081, People's Republic of China
^t Hunan University, Changsha 410082, People's Republic of China
^u Indian Institute of Technology Madras, Chennai 600036, India
^v Indiana University, Bloomington, IN 47405, USA
^w INFN Laboratori Nazionali di Frascati, I-00044, Frascati, Italy
^x INFN and University of Perugia, I-06100, Perugia, Italy
^y INFN Sezione di Ferrara, I-44122, Ferrara, Italy
^z University of Ferrara, I-44122, Ferrara, Italy
^{aa} Institute of Modern Physics, Lanzhou 730000, People's Republic of China
^{ab} Institute of Physics and Technology, Peace Ave. 54B, Ulaanbaatar 13330, Mongolia
^{ac} Jilin University, Changchun 130012, People's Republic of China
^{ad} Johannes Gutenberg University of Mainz, Johann-Joachim-Becher-Weg 45, D-55099 Mainz, Germany
^{ae} Joint Institute for Nuclear Research, 141980 Dubna, Moscow region, Russia
^{af} Justus-Liebig-Universitaet Giessen, II. Physikalisches Institut, Heinrich-Buff-Ring 16, D-35392 Giessen, Germany
^{ag} KVI-CART, University of Groningen, NL-9747 AA Groningen, the Netherlands
^{ah} Lanzhou University, Lanzhou 730000, People's Republic of China
^{ai} Liaoning Normal University, Dalian 116029, People's Republic of China
^{aj} Liaoning University, Shenyang 110036, People's Republic of China
^{ak} Nanjing Normal University, Nanjing 210023, People's Republic of China
^{al} Nanjing University, Nanjing 210093, People's Republic of China
^{am} Nankai University, Tianjin 300071, People's Republic of China
^{an} Peking University, Beijing 100871, People's Republic of China
^{ao} Qufu Normal University, Qufu 273165, People's Republic of China
^{ap} Shandong Normal University, Jinan 250014, People's Republic of China
^{aq} Shandong University, Jinan 250100, People's Republic of China
^{ar} Shanghai Jiao Tong University, Shanghai 200240, People's Republic of China
^{as} Shanxi Normal University, Linfen 041004, People's Republic of China
^{at} Shanxi University, Taiyuan 030006, People's Republic of China
^{au} Sichuan University, Chengdu 610064, People's Republic of China
^{av} Soochow University, Suzhou 215006, People's Republic of China
^{aw} Southeast University, Nanjing 211100, People's Republic of China
^{ax} State Key Laboratory of Particle Detection and Electronics, Beijing 100049, Hefei 230026, People's Republic of China
^{ay} Sun Yat-Sen University, Guangzhou 510275, People's Republic of China
^{az} Tsinghua University, Beijing 100084, People's Republic of China
^{ba} Ankara University, 06100 Tandogan, Ankara, Turkey
^{bb} Istanbul Bilgi University, 34060 Eyup, Istanbul, Turkey
^{bc} Uludag University, 16059 Bursa, Turkey
^{bd} Near East University, Nicosia, North Cyprus, Mersin 10, Turkey
^{be} University of Chinese Academy of Sciences, Beijing 100049, People's Republic of China
^{bf} University of Hawaii, Honolulu, HI 96822, USA
^{bg} University of Jinan, Jinan 250022, People's Republic of China
^{bh} University of Manchester, Oxford Road, Manchester, M13 9PL, United Kingdom
^{bi} University of Minnesota, Minneapolis, MN 55455, USA
^{bj} University of Muenster, Wilhelm-Klemm-Str. 9, 48149 Muenster, Germany
^{bk} University of Oxford, Keble Rd, Oxford, OX13RH, United Kingdom
^{bl} University of Science and Technology Liaoning, Anshan 114051, People's Republic of China
^{bm} University of Science and Technology of China, Hefei 230026, People's Republic of China
^{bn} University of South China, Hengyang 421001, People's Republic of China
^{bo} University of the Punjab, Lahore-54590, Pakistan
^{bp} University of Turin, I-10125, Turin, Italy
^{bq} University of Eastern Piedmont, I-15121, Alessandria, Italy
^{br} INFN, I-10125, Turin, Italy
^{bs} Uppsala University, Box 516, SE-75120 Uppsala, Sweden
^{bt} Wuhan University, Wuhan 430072, People's Republic of China
^{bu} Xinyang Normal University, Xinyang 464000, People's Republic of China
^{bv} Zhejiang University, Hangzhou 310027, People's Republic of China
^{bw} Zhengzhou University, Zhengzhou 450001, People's Republic of China

ARTICLE INFO

Article history:

Received 11 October 2021

Received in revised form 18 April 2022

Accepted 16 May 2022

ABSTRACT

The Born cross sections of $e^+e^- \rightarrow \Sigma^0 \bar{\Sigma}^0$ are measured at center-of-mass energies from 2.3864 to 3.0200 GeV using data samples with an integrated luminosity of 328.5 pb^{-1} collected with the BESIII detector operating at the BEPCII collider. The analysis makes use of a novel reconstruction method for energies near production threshold, while a single-tag method is employed at other center-of-mass

Available online 20 May 2022
 Editor: M. Doser

Keywords:
 BESIII
 Σ^0 hyperon
 Born cross section
 Form factor

energies. The measured cross sections are consistent with earlier results from BaBar, with a substantially improved precision. The cross-section lineshape can be well described by a perturbative QCD-driven energy function. In addition, the effective form factors of the Σ^0 baryon are determined. The results provide precise experimental input for testing various theoretical predictions.

© 2022 The Author(s). Published by Elsevier B.V. This is an open access article under the CC BY license (<http://creativecommons.org/licenses/by/4.0/>). Funded by SCOAP³.

1. Introduction

Studies to gain a better understanding of the internal structure of the nucleons have been ongoing ever since the discovery of their non-pointlike nature [1]. As discussed in Refs. [2–4], the electromagnetic form factors (EMFFs) are fundamental nucleon observables that are closely related to their internal structure and dynamics. Further insight into nucleon structure can also be obtained by studying hyperons that contain one or more strange quarks [5,6].

Due to their instability, the EMFFs of hyperons are mostly studied in the time-like region, e.g. via electron-positron annihilation into a hyperon-antihyperon pair. Experimentally, many unexpected features have been observed concerning the reaction $e^+e^- \rightarrow B\bar{B}$ close to their production thresholds, where B denotes a baryon [7]. In the charged-baryon sector, a steep rise in the cross section near the production threshold followed by a plateau is observed for $e^+e^- \rightarrow p\bar{p}$ [8,9] and $e^+e^- \rightarrow \Lambda_c^+\bar{\Lambda}_c^-$ [10]. In the neutral baryon sectors, a non-vanishing cross section near threshold has been observed for $e^+e^- \rightarrow n\bar{n}$ [11] and $e^+e^- \rightarrow \Lambda\bar{\Lambda}$ [12]. These abnormal threshold effects have been extensively discussed in the literature, where they are interpreted as being caused by final-state interactions [13], bound states or unobserved meson resonances [14], or attractive and repulsive Coulomb forces among quarks [15]. To decide between these hypotheses and gain a better understanding of the nature of these effects, more measurements are required on baryon-pair production, especially near production threshold.

Recently, the reactions $e^+e^- \rightarrow \Sigma^\pm\bar{\Sigma}^\mp$ [16] and $e^+e^- \rightarrow \Xi\bar{\Xi}$ [17] have been investigated at BESIII with an energy-scan approach. No significant threshold effects are observed in these processes [16,17]. Instead, a perturbative-QCD driven function can describe the cross section lineshapes well. In addition, it is found that the cross sections for $e^+e^- \rightarrow \Sigma^-\bar{\Sigma}^+$ are consistently smaller than those for $e^+e^- \rightarrow \Sigma^+\bar{\Sigma}^-$, and the corresponding EMFFs of Σ^\pm are proportional to the incoherent sum of the squared charges of their valence quarks, $\sum_q Q_q^2$ with $q = u, d, s$ quarks. Thus, it is interesting to measure the Born cross section of $e^+e^- \rightarrow \Sigma^0\bar{\Sigma}^0$ near the production threshold and validate whether the same asymmetry appears in the EMFFs of Σ^0 in the same energy region. In addition, the study of $e^+e^- \rightarrow \Sigma^0\bar{\Sigma}^0$ provides important experimental input for testing the diquark correlation model [18], which predicts that the cross section of $e^+e^- \rightarrow \Sigma^0\bar{\Sigma}^0$ reaction is significantly suppressed compared to that of $e^+e^- \rightarrow \Lambda\bar{\Lambda}$. Previous measurements of $e^+e^- \rightarrow \Sigma^0\bar{\Sigma}^0$ have been performed at BaBar via an initial-state radiation (ISR) approach [19]. However, the uncertainty on these measurements is too large to address the above questions. Thus, it is important to study the $e^+e^- \rightarrow \Sigma^0\bar{\Sigma}^0$ reaction at collision energies at and above its production threshold with improved precision.

In this Letter, we present a measurement of the process $e^+e^- \rightarrow \Sigma^0\bar{\Sigma}^0$ at BESIII, using data samples corresponding to an integrated luminosity of 328.5 pb^{-1} at center-of-mass (c.m.) energies ranging from 2.3864 to 3.0200 GeV [20]. A novel method is applied to reconstruct the secondary particles from antiproton interactions for signal process near production threshold [12], and a single-tag method that reconstructs $\Sigma^0 \rightarrow \gamma\Lambda$ and $\Lambda \rightarrow p\pi^-$ is performed for other c.m. energies. The charge-conjugate state

of the Σ^0 mode is always implied when discussing the single-tag method.

2. Detector and Monte Carlo simulation

The BESIII detector is a magnetic spectrometer [21] located at Beijing Electron Positron Collider (BEPCII). The cylindrical core of the BESIII detector covers 93% of the full solid angle and consists of a helium-based multilayer drift chamber (MDC), a plastic scintillator time-of-flight system (TOF), and a CsI(Tl) electromagnetic calorimeter (EMC). The subdetectors are enclosed in a superconducting solenoid magnet with a field strength of 1.0 T. The solenoid is supported by an octagonal flux-return yoke with resistive plate counter muon-identifier modules interleaved with steel. The momentum resolution of charged particles is 0.5% at 1 GeV, and the energy loss (dE/dx) measurement provided by the MDC has a resolution of 6% for the electrons from Bhabha scattering. The energy resolution for the photons is 2.5% (5%) at 1 GeV in the barrel (end cap) of the EMC. The time resolution of the TOF is 68 ps (110 ps) in the barrel (end-cap) region.

Simulated Monte Carlo (MC) samples generated with a GEANT4-based [22] package, which includes the geometric description of the BESIII detector, and the detector response, are used to determine detection efficiency and to estimate background contributions. In this analysis, the generator software package CONEXC [23] is used to simulate the signal MC samples $e^+e^- \rightarrow \Sigma^0\bar{\Sigma}^0$, and calculate the corresponding correction factors for higher-order processes with one radiative photon. The angular amplitude of this process is taken to be uniform in phase space (PHSP) at $\sqrt{s} = 2.3864 \text{ GeV}$ due to the by-definition equality of electric (G_E) and magnetic (G_M) form factors (FFs) at threshold, and is distributed according to the differential amplitude presented in Ref. [24] at other c.m. energies. The studies of $e^+e^- \rightarrow \Sigma^0\bar{\Sigma}^0$ near threshold employ a sample in which the subsequent decay modes of both Σ^0 and $\bar{\Sigma}^0$ are simulated using EVTGEN [25] with an exclusive decay chain $e^+e^- \rightarrow \Sigma^0\bar{\Sigma}^0 \rightarrow \gamma\gamma\Lambda\bar{\Lambda} \rightarrow \gamma\gamma p\bar{p}\pi^+\pi^-$. For the higher energy studies of $e^+e^- \rightarrow \Sigma^0\bar{\Sigma}^0$ with a single-tag method, the decay mode of $\Sigma^0 \rightarrow \gamma\Lambda$ with subsequent decay $\Lambda \rightarrow p\pi^-$ is simulated, while the $\bar{\Sigma}^0$ is allowed to decay inclusively according to the branching fractions reported by the Particle Data Group (PDG) [26,27]. Large simulated samples of generic $e^+e^- \rightarrow$ hadrons events implemented by the LUNDARLW generator [28] are used to estimate possible backgrounds. Final-state radiation (FSR) from charged final-state particles is incorporated using the PHOTOS package [29]. Backgrounds coming from the QED processes $e^+e^- \rightarrow l^+l^-$ ($l = e, \mu$) and $e^+e^- \rightarrow \gamma\gamma$ are investigated with BABAYAGA [30], while BESTWOGAM [31] is used for two-photon processes. The dominant background channels, $e^+e^- \rightarrow \Lambda\bar{\Lambda} \rightarrow p\bar{p}\pi^+\pi^-$ and $e^+e^- \rightarrow \Lambda\bar{\Sigma}^0 + c.c.$, are generated exclusively using the phase-space CONEXC [23] generator. The background Σ^0 and Λ particles are simulated in the $\Sigma^0 \rightarrow \gamma\Lambda$ and $\Lambda \rightarrow p\pi^-$ decay modes.

3. Formalism

Under the one-photon exchange approximation, the Born cross section for the process $e^+e^- \rightarrow B\bar{B}$, where B is a spin-1/2 baryon, can be expressed in terms of G_E and G_M FFs [32] as

$$\sigma^B(s) = \frac{4\pi\alpha^2\beta C}{3s} \left[|G_M(s)|^2 + \frac{1}{2\tau} |G_E(s)|^2 \right]. \quad (1)$$

Here, α is the fine-structure constant, s is the square of the c.m. energy, $\beta = \sqrt{1 - 1/\tau}$ is a phase-space factor, $\tau = s/4m_B^2$, m_B is the baryon mass and C is the Coulomb enhancement factor that accounts for the $B\bar{B}$ final-state interaction [33,34]. The factor C is equal to unity for pairs of neutral baryons and $y/(1 - e^{-y})$ with $y = \pi\alpha(1 + \beta^2)/\beta$ for pairs of charged baryons. From Eq. (1), it follows that the Born cross section of $e^+e^- \rightarrow B\bar{B}$ is non-zero at the production threshold ($\beta \rightarrow 0$) for charged baryon pairs, while it should vanish at the threshold for neutral baryon pairs.

The magnitude of the effective form factor $|G_{\text{eff}}|$ is defined by the combination of the G_E and G_M FFs [35] as

$$|G_{\text{eff}}(s)| \equiv \sqrt{\frac{2\tau |G_M(s)|^2 + |G_E(s)|^2}{2\tau + 1}}. \quad (2)$$

Experimentally, the Born cross section of $e^+e^- \rightarrow \Sigma^0\bar{\Sigma}^0$ can be determined by

$$\sigma^B(s) = \frac{N_{\text{obs}}}{\mathcal{L}(1 + \delta^r) \frac{1}{|1 - \Pi|^2} \varepsilon \mathcal{B}}, \quad (3)$$

where N_{obs} is the yield of signal events in data, \mathcal{L} is the integrated luminosity, $(1 + \delta^r)$ is the ISR correction factor, $\frac{1}{|1 - \Pi|^2}$ is the vacuum polarization factor [36], and ε is the detection efficiency determined from simulated MC events. The factor \mathcal{B} is the product of the relevant daughter branching fractions, i.e., $\mathcal{B} = \mathcal{B}(\Lambda \rightarrow p\pi^-) \cdot \mathcal{B}(\bar{\Lambda} \rightarrow \bar{p}\pi^+)$ for exclusive MC near production threshold, and $\mathcal{B} = \mathcal{B}(\Lambda \rightarrow p\pi^-)$ for semi-inclusive MC at other c.m. energies. We note that as the branching fraction of the decay $\Sigma^0 \rightarrow \gamma\Lambda$ is 100%, we omit it from the expression for \mathcal{B} [27]. To determine reliable detection efficiencies and ISR factors [37], the Born cross sections used as input in the generator have been iterated until the product $(1 + \delta^r) \cdot \varepsilon$ has converged, defined as an iteration leading to a relative change of less than 1.0%. It is noteworthy that the Born cross sections used in the event generator are replaced by the results measured in this analysis.

With the Born cross section obtained experimentally, $|G_{\text{eff}}|$ can be determined through substitution of Eq. (1) into Eq. (2) to yield

$$|G_{\text{eff}}(s)| = \sqrt{\frac{\sigma^B(s)}{\frac{4\pi\alpha^2\beta C}{3s} \left[1 + \frac{1}{2\tau} \right]}}, \quad (4)$$

which is proportional to the square root of the Born cross section.

4. Data analysis at $\sqrt{s} = 2.3864$ and 2.3960 GeV

In this section, the process $e^+e^- \rightarrow \Sigma^0\bar{\Sigma}^0$ at $\sqrt{s} = 2.3864$ GeV, which is approximately 1.2 MeV above production threshold, and at $\sqrt{s} = 2.3960$ GeV is selected with the final state topology $\gamma\gamma p\bar{p}\pi^+\pi^-$. Due to the low momenta of final state particles near threshold and the small PHSP in $\Sigma^0(\bar{\Sigma}^0)$ decays, the proton and antiproton in the final states are not easily detected in the MDC. Furthermore, the detection efficiency of signal photons is low at these energies, and there is a high multiplicity of background photons. Thus, we do not search for the protons and the photons from

the signal channel. Instead, we reconstruct the soft pions and secondary products of antiproton interactions, following the method described in Ref. [12].

Although the final-state pions from the signal channel have a low momentum, and, thereby, a low detection efficiency, these charged particles can be still detected by the MDC. A charged track must fulfill the condition $|\cos\theta| < 0.93$, where θ is the polar angle with respect to the direction of the positron beam. The closest approach to the interaction point (IP) is required to be less than 10 cm along the beam direction ($|V_z| < 10$ cm), and less than 1 cm in the plane perpendicular to the beam ($V_{xy} < 1$ cm). If a charged track does not satisfy the above requirements, it is considered to be a not good (NG) charged track. Only the dE/dx information obtained from the MDC is used to compute particle identification (PID) confidence levels for a pion, kaon and proton hypotheses, as the low momentum of the particles under consideration prevents them reaching the TOF system. Each charged track is assigned to the particle type with the highest confidence level. Exactly two good charged tracks and at least two NG tracks are required in each candidate event. The candidate events are required to have two good charged tracks identified as π^- and π^+ , associated with the pions from the $\Lambda(\bar{\Lambda})$ decay. Due to the vertex resolution of low momentum charged tracks near threshold, the detector unable to distinguish between these soft pions comes from two different Λ decay vertices. To improve the pions momentum resolution and suppress the beam-associated background, the two charged pion tracks are constrained to a common decay vertex by applying a vertex fit. The transverse distance of the decay vertex from the IP is required to be less than 2 cm.

The antiproton from the signal decay interacts with the nucleons of the detector material, mostly in the beam-pipe, and produces several secondary particles. To identify the secondary particles produced from the antiproton, at least two NG tracks are required. A vertex fit is then applied to those high momenta secondary tracks. Furthermore, the transverse distance of the decay vertex (R_{xy}) with a resolution of 0.12 cm from the beam pipe is required to lie within (1, 5) cm. This range is set following the results of a signal MC study which shows the majority of decay vertices to be at around 3 cm, which is the radius of beam-pipe.

It is further required that $\theta_{\pi^+\pi^-} \in (20^\circ, 170^\circ)$, where $\theta_{\pi^+\pi^-}$ is the opening angle between the π^+ and the π^- , to remove cosmic rays and γ -conversion ($\gamma \rightarrow e^+e^-$) events. To suppress the combinatorial background, the momentum of π^- tracks is required to be located in the signal region (0.08, 0.12) GeV/c. The momentum of π^+ tracks is shown in Fig. 1.

Potential sources of residual contamination that survive the selection are investigated by studying the generic hadronic MC samples with an event type analysis tool, TopoAna [38]. The main peaking background originates from $e^+e^- \rightarrow \Lambda\bar{\Lambda}$ and $e^+e^- \rightarrow \bar{\Lambda}\Sigma^0 + c.c.$, which are decays with one or two fewer photons than the signal final state. For these processes, dedicated exclusive MC samples are generated to estimate their contributions in the signal region. It is noted that the momentum of pion tracks from Λ 's decay can be used to distinguish the $e^+e^- \rightarrow \Sigma^0\bar{\Sigma}^0$ signal channel from the exclusive background $e^+e^- \rightarrow \Lambda\bar{\Lambda}$ and $e^+e^- \rightarrow \bar{\Lambda}\Sigma^0 + c.c.$ channels, as pion is mono-energetic in $e^+e^- \rightarrow \Sigma^0\bar{\Sigma}^0$ with almost standing-still Σ^0 near its production threshold. The contribution from beam-associated background events is estimated from a sample of data collected with separated beams at $\sqrt{s} = 2.6444$ GeV. The background events are normalized according to beam-time. Detailed MC studies indicate that the generic hadronic MC samples are distributed smoothly after removing the above exclusive background channels, as well as the beam-associated background in the region of interest, as illustrated in Fig. 1.

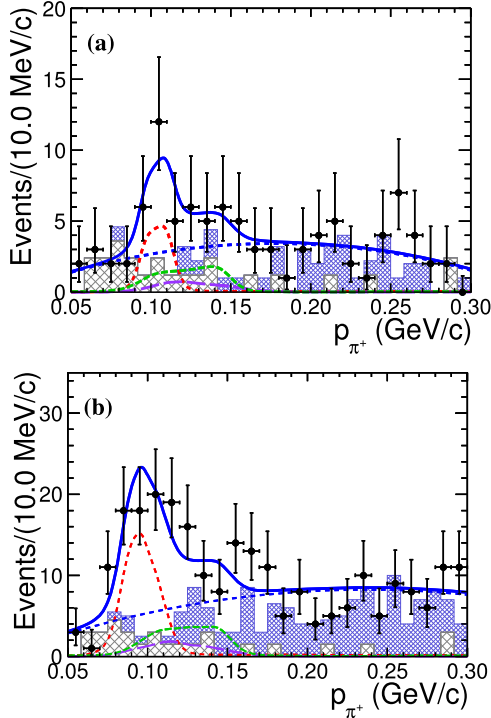


Fig. 1. Momentum distributions of reconstructed π^+ tracks for selected $e^+e^- \rightarrow \Sigma^0 \bar{\Sigma}^0$ events at (a) $\sqrt{s} = 2.3864$ GeV and (b) $\sqrt{s} = 2.3960$ GeV. Dots with error bars (in black) are from data; hatched histograms (in grey and magenta) are the combinatorial background events of normalized beam-related background and generic hadronic MC samples after removing the peaking exclusive background channels. The solid blue curve represents the total fit, red dashed curve the signal, dashed blue curve the non-peaking backgrounds, whereas the long dashed violet curve and dashed green curve are the fixed background lineshapes from the exclusive MC samples of $e^+e^- \rightarrow \Lambda \bar{\Lambda}$ and $e^+e^- \rightarrow \Lambda \bar{\Sigma}^0 + c.c.$, respectively.

To determine the signal yields, an unbinned maximum-likelihood fit is performed to the momentum of π^+ tracks (p_{π^+}). The signal probability-density function (PDF) is described with a MC-simulated at 2.3864 GeV, while at 2.3960 GeV convolved with a Gaussian function to compensate for possible mass-resolution differences between data and MC simulation. The parameters of the Gaussian function are free in the fit, and corresponding Gaussian smearing fit values of the mean $\mu = (-0.1 \pm 3.9)$ MeV, and the width $\sigma = (1.0 \pm 0.7)$ MeV are respectively. The backgrounds from $e^+e^- \rightarrow \Lambda \bar{\Lambda}$ and $e^+e^- \rightarrow \Lambda \bar{\Sigma}^0 + c.c.$ are described by the MC-determined shapes, where the yields normalized according to the luminosity and their cross sections [12] are fixed in the fit. The PDF for other generic hadronic MC samples and beam-associated backgrounds are described by a second-order polynomial function. The fit results at $\sqrt{s} = 2.3864$ and 2.3960 GeV are shown in Fig. 1. The statistical significances of the signals in p_{π^+} distributions at $\sqrt{s} = 2.3864$ and 2.3960 GeV are found to be 2.3σ and 4.5σ , respectively, which are determined according to Wilks' theorem [40] from the differences of the log-likelihood values and degrees of freedom with and without considering the signal process in the fits. As a cross-check, an alternative two-dimensional fit is performed to the momentum of π^+ and π^- tracks at each energy point, which is found to give compatible results. The Born cross sections of $e^+e^- \rightarrow \Sigma^0 \bar{\Sigma}^0$ and effective FFs of Σ^0 at $\sqrt{s} = 2.3864$ and 2.396 GeV can be determined using Eq. (3) and Eq. (4). The results and the inputs used in the calculation are summarized in Table 3.

Since the statistical significance of signal events is less than 3σ at 2.3864 GeV, the upper limit (U.L.) on the number of signal events ($N_{U.L.}$) is estimated at the 90% confidence level (C.L.)

using a Bayesian method [39]. We separate the systematic uncertainties into two categories: correlated uncertainties associated with the background shapes and fit range, and the remainder that are considered as uncorrelated. To take into account the uncorrelated uncertainties related to the fit procedure, two alternative fit scenarios are considered: (1) changing the momentum range by 5 MeV/c; and (2) replacing the second-order polynomial function with the exact background distribution seen in Fig. 1. We consider all combinations of the two scenarios and select the likelihood curve with the maximum $N_{U.L.}$ as a conservative estimate. The selected likelihood distribution is then smeared by the remaining so-called correlated uncertainties, whose components are described below. The calculation of the U.L. on the Born cross section and effective FF at the 90% C.L. is performed analogously by replacing the N_{obs} with $N_{U.L.}$, as shown in Table 3.

Several sources of systematic uncertainties are considered in the measurement of the Born cross section near the production threshold. The π^\pm tracking (PID) efficiencies are studied using a control sample of $J/\psi \rightarrow p\bar{p}\pi^+\pi^-$ events. The corresponding systematic uncertainties are estimated as 4.6% (2.0%). Alternative fits are performed to study the uncertainty from the fit procedure. These include varying the fitting range, varying the signal shape by fixing the resolution of the convolved Gaussian to be $\pm 1\sigma$ different from its nominal value, changing the background PDF from a second order polynomial function to the background shape from the generic hadronic MC samples combined with the contribution from the beam-related background and varying the cross section of fixed backgrounds lineshapes within the uncertainty of normalized backgrounds events.

Possible biases due to the various rejection windows are assessed by varying the criteria above and below the nominal selection, as described in Ref. [41,42]. For each systematic variation, the parameters values are re-obtained, $x_{test} \pm \sigma_{test}$ and the changes evaluated compared to the nominal values, $\Delta x = |x_{nom.} - x_{test}|$. Also calculated are the uncorrelated uncertainties, $\sigma_{uc.} = \sqrt{|\sigma_{nom.}^2 - \sigma_{test}^2|}$, where $\sigma_{nom.}$ and σ_{test} correspond to the fit uncertainties of the nominal and systematic test results, respectively. A systematic uncertainty is assigned, if the ratio $r = \Delta x / \sigma_{uc.}$ shows a trending behavior and is larger than two. The effect of the R_{xy} is tested by varying the boundaries of the rejection windows from 0.4 to 1.6 cm (lower side) and 4.4 to 5.6 cm (higher side) with respect to the nominal selection. Since the corresponding normalized shift is $r < 2$, no uncertainty of the selection efficiency for the antiproton is assigned. The effect of the $\theta_{\pi^+\pi^-}$ veto is tested by varying the boundaries of the rejection windows from 16° to 24° (lower side) and 166° to 174° (higher side) with respect to the nominal selection. Since the corresponding normalized shift is $r < 2$, no associated uncertainty is assigned. The uncertainty due to the cross section lineshape is negligible as well, as is discussed below in Sec. 5. The c.m. energy spread of BEPCII is 0.5 MeV, which is measured by Beam Energy Measurement System [43]. Since the BEMS is not operated during the data taking from 2.3864 to 3.0200 GeV, however, we can take the comparison during data taking of J/ψ scan as a reference [20]. It is noted that the uncertainty from the beam energy spread is negligible in this analysis. However, the conservative estimate of the uncertainty due to the variation of c.m. energy and energy spread, while assuming the uncertainty of c.m. energy to be 1.5 MeV. The yielding uncertainties in the cross section are 1.1% and 5.6%, and the corresponding uncertainties in the effective FF are 17% and 3.2%, respectively, at 2.3864 and 2.3960 GeV, where the larger uncertainty in the effective FF at 2.3864 GeV is due to the rapid variation of the velocity factor β . The integrated luminosity is determined with large angle Bhabha events with an uncertainty of 1.0% [20]. All these systematic uncertainties are treated as uncorrelated and summed in quadrature,

Table 1
Systematic uncertainties on the Born cross section measurements (in%).

Source	2.3864	2.3960
Luminosity	1.0	1.0
Tracking	4.6	4.6
PID	2.0	2.0
Antiproton	—	—
Background shape	5.4	2.0
Fitting range	1.3	7.9
Fixed background shape	4.8	2.4
ISR factor	—	—
Opening angle	—	—
Beam energy	1.1	5.6
Total	9.0	11.4

giving a total uncertainty of 9.0% and 11.4% for the Born cross section at $\sqrt{s} = 2.3864$ and 2.3960 GeV, as summarized in Table 1. As the effective FF is proportional to the square root of the Born cross section, the corresponding systematic uncertainty on this quantity is half that of the uncertainty on the Born cross section.

5. Data analysis from $\sqrt{s} = 2.5000$ to 3.0200 GeV

As the full reconstruction method for selecting the $e^+e^- \rightarrow \Sigma^0 \bar{\Sigma}^0$ events has a low reconstruction efficiency, a single-tag Σ^0 baryon technique is employed at energies of $\sqrt{s} = 2.5000$ GeV and above. We fully reconstruct the Σ^0 -prong in the $\gamma\Lambda$ decay mode with $\Lambda \rightarrow p\pi^-$.

Charged tracks are reconstructed within $|\cos\theta| < 0.93$ and are required to satisfy $|V_z| < 30$ cm and $V_{xy} < 10$ cm. The combined information from dE/dx and TOF is used to form particle-identification (PID) confidence levels for π, K and p hypotheses. Each track is assigned to the particle type corresponding to the highest confidence level. Candidate events with at least two charged tracks identified as a proton and a pion are kept for further analysis. The photon candidate is required to be within the barrel region ($|\cos\theta| < 0.8$) of the EMC with deposited energy of at least 25 MeV, and within the end-cap regions ($0.86 < |\cos\theta| < 0.92$) with at least 50 MeV. In order to suppress electronic noise and showers unrelated to the event, the EMC time difference from the event start time is required to be within (0, 700) ns. At least one photon is required in this analysis.

Λ candidates are reconstructed with a vertex fit to all the identified $p\pi^-$ combinations. A secondary-vertex fit [44] is then employed for the Λ candidate and events are kept if the decay length, *i.e.* the distance from the production vertex to the decay vertex, is greater than zero. A mass window of $|M_{p\pi^-} - m_\Lambda| < 6$ MeV/ c^2 is required to select Λ candidates, where m_Λ is the known Λ mass from the PDG [27]. In addition, the value of χ^2 from the secondary vertex fit is required to be less than 20, determined by optimizing the figure of merit $N_S/\sqrt{N_S + N_B}$ based on MC simulation, where N_S is the number of signal MC events and N_B is the number of background events in the generic hadronic MC sample normalized according to integrated luminosity and cross section. All combinations of the Λ and photon candidates are considered, and that combination with the minimum value of $|p_{\Sigma^0} - p_{\text{exp.}}|$ is chosen to determine the photon from Σ^0 decay, where p_{Σ^0} and $p_{\text{exp.}}$ are the measured and expected momentum of Σ^0 , defined as $p_{\text{exp.}} \equiv \sqrt{s/4 - m_{\Sigma^0}^2}$, with m_{Σ^0} the mass of Σ^0 from the PDG [27]. A momentum window $|p_{\Sigma^0} - p_{\text{exp.}}| < 3.5\sigma_p$, is then applied to select the $\gamma\Lambda$ candidate. Here both momenta are defined in the c.m. frame system, and σ_p is the corresponding optimized momentum resolution, which is about 7 MeV/ c at each energy point.

The generic hadronic MC samples are used to study possible peaking-background contributions. After applying the same

requirements as used for the data, the surviving background is found to originate from e^+e^- annihilation events with the same final state particles as the signal process, with one or more additional π^0 , and with one less photon. These background processes are mainly from contributions including intermediate states such as Λ, Δ , and Σ baryons. For the dominant backgrounds such as $e^+e^- \rightarrow \Lambda\bar{\Lambda}$ and $e^+e^- \rightarrow \bar{\Lambda}\Sigma^0 + c.c.$, dedicated exclusive MC samples are generated to estimate their contributions to the $\gamma\Lambda$ mass spectrum. A few peaking background events from the process $e^+e^- \rightarrow \bar{\Lambda}\Sigma^0 + c.c.$ contribute to the $\gamma\Lambda$ mass region and their normalized contribution is shown in Fig. 2. There is a negligible contribution from $e^+e^- \rightarrow \Lambda\bar{\Lambda}$ events.

The signal yields for $e^+e^- \rightarrow \Sigma^0 \bar{\Sigma}^0$ at each energy point are determined by an unbinned maximum likelihood fit to the $M_{\gamma\Lambda}$ spectrum. The PDF is described with the MC-simulated shape convolved with a Gaussian function to account for the mass-resolution difference between data and the MC simulation. The parameters of the Gaussian function are floating in the fit, and the corresponding smearing fit values of the mean and the width are presented in Fig. 2 at each energy point. A second-order polynomial function describes the non-peaking background PDF, whereas the peaking backgrounds are modeled with the MC-determined lineshapes and their respective yields fixed in the fits. Fit results at $\sqrt{s} = 2.3960, 2.5000, 2.6444, 2.6464, 2.9000$ and 2.9884 GeV are shown in Fig. 2. As the single-tag method leads to the double counting effect of the $\Sigma^0 \bar{\Sigma}^0$ final-state. It is rather possible that a small fraction of events of both Σ^0 and $\bar{\Sigma}^0$ prongs are reconstructed, which introduces the double counting while fitting the $M_{\gamma\Lambda}$ spectrum. A correction factor of 1.09 for $\sqrt{s} = 2.6444$ and 2.6464 GeV is applied to the statistical uncertainty to account for this effect based on MC simulation [17], while for other energy points, the correction factor is estimated to be 1.07. The number of observed events are summarized in Table 3. The Born cross sections and corresponding effective FFs are determined using Eq. (3) and Eq. (4). The quantities used in the Born cross sections and effective FFs calculations for $e^+e^- \rightarrow \Sigma^0 \bar{\Sigma}^0$ are summarized in Table 3. It should be noted that the data at c.m. energies 2.9500, 2.9810, 3.0000 and 3.0200 GeV are combined to a single luminosity-weighted energy point of 2.9884 GeV on account of the limited size of each sub-sample.

Sources of systematic uncertainties related to the cross-section measurement include those associated with the Λ reconstruction, the photon detection, the momentum window, the fitting method, the cross section lineshape, the angular distribution, the relative phase and the luminosity measurement. The systematic uncertainty on the Λ reconstruction efficiency, associated with the tracking/PID, decay length and mass window requirements is estimated to be 4.5% [12]. The uncertainty on the photon-detection efficiency is assigned by considering a control sample of the decay $J/\psi \rightarrow \pi^+\pi^-\pi^0$ and is found to be 1.0% for each photon [45]. The p_{Σ^0} veto is tested by varying the selection window, $|p_{\Sigma^0} - p_{\text{exp.}}|$ from $2\sigma_p$ to $6\sigma_p$ with the same method as explained above in Sec. 4, and taking the largest deviation from the nominal result as a conservative estimate of the corresponding uncertainty. Alternative fits are performed to study the uncertainty from the fit procedure. These include varying the fitting range, changing the background PDF from a second-order polynomial to a third-order polynomial function and varying the cross section of fixed background lineshape within the uncertainty of normalized background events. The uncertainty associated with the description of the signal lineshape is estimated by parameterizing the lineshape in each iteration according to the pQCD power-law function and sampling 500 lineshapes according to the uncertainty of the parameters and their covariance matrix. The variation in result is found to be much less than 1% and can be neglected. In order to investigate the bias coming from the angular distribution, the analysis is repeated with

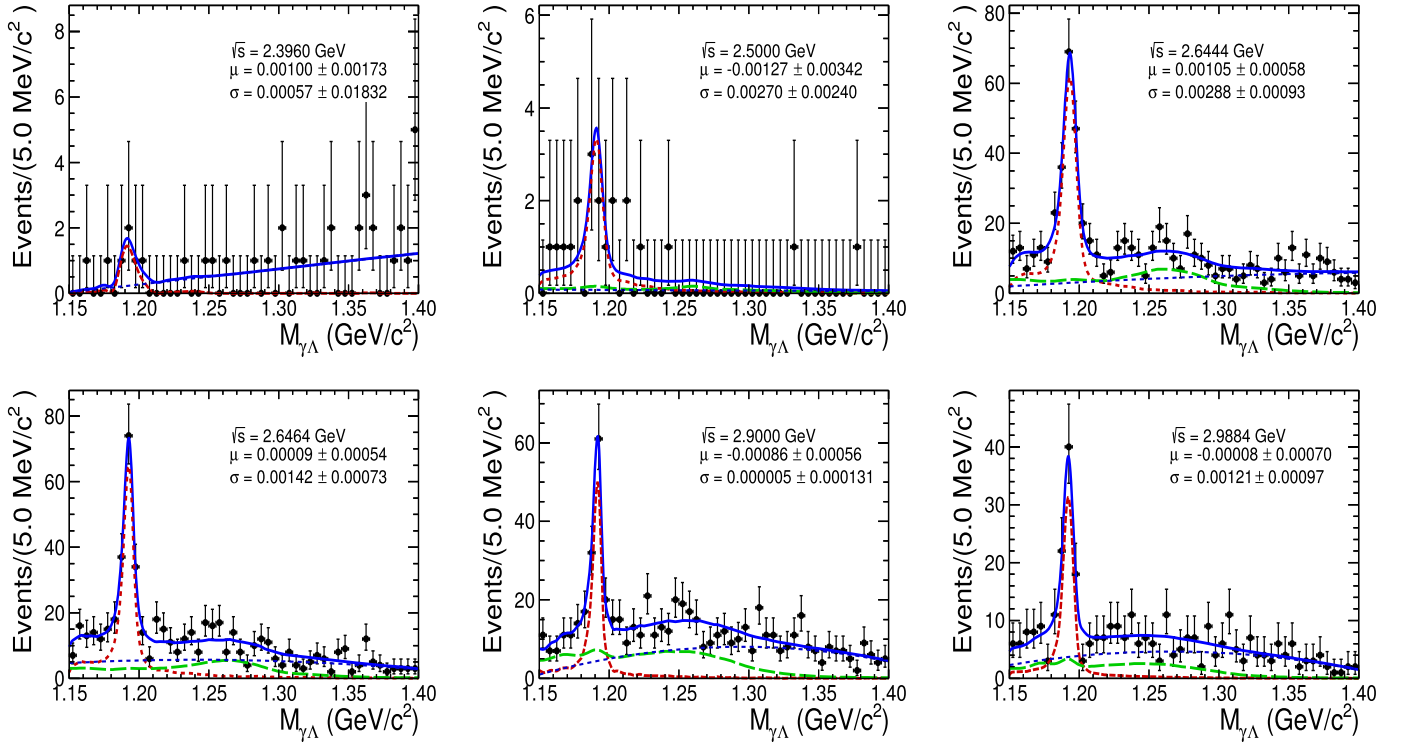


Fig. 2. Fit result of the mass spectra $M_{\gamma\Lambda}$ at each energy point. Dots with error bars are from data, the solid blue curve represents the overall fit, red dashed curve the signal, dashed blue curve the non-peaking backgrounds, and the long dashed green curve is the fixed background lineshape from a MC sample $e^+e^- \rightarrow \Lambda \bar{\Sigma}^0 + c.c.$, respectively. The mean μ and width σ in each legend represents the Gaussian smearing fit values in unit of GeV at each energy.

Table 2
Systematic uncertainties on the Born cross section measurements (in%).

Source	2.5000	2.6444	2.6464	2.9000	2.9884
Luminosity	1.0	1.0	1.0	1.0	1.0
Λ reconstruction	4.5	4.5	4.5	4.5	4.5
Photon reconstruction	1.0	1.0	1.0	1.0	1.0
Momentum window	3.6	2.0	3.4	3.4	2.2
Background shape	9.9	1.0	0.6	1.0	1.5
Fitting range	2.9	3.0	2.8	3.1	1.2
Fix background shape	0.2	0.5	0.6	0.7	1.7
ISR factor	—	—	—	—	—
Angular distribution	1.8	1.1	1.9	2.5	1.4
Relative phase	—	—	—	—	—
Total	12.0	6.1	6.8	7.2	6.0

the two extreme values of $G_E = 0$ and $G_M = 0$ and the difference in the resulting efficiencies divided by a factor of $\sqrt{12}$ is taken as the uncertainty [41]. In addition, to account for effects arising from the uncertainty in the relative phase ($\Delta\Phi$) between the G_E and G_M FFs, we consider two extreme cases with $\Delta\Phi = 0^\circ$ and 90° , and find the difference in results to be negligible. The integrated luminosity is determined with large-angle Bhabha events with an uncertainty of 1.0% [20]. All the uncertainties are considered uncorrelated and summed in quadrature. They are between 6.1% and 12.0% of the cross sections, depending on the c.m. energy as listed in Table 2.

As a cross-check, we compare the Born cross-section result measured at $\sqrt{s} = 2.3960$ GeV from the single-tag method with that of the novel approach described in Sec. 4. It is found that both results are consistent within the uncorrelated uncertainty. The result obtained by the novel approach is considered as nominal at this energy point, since it leads to a smaller uncertainty on the cross section than the result obtained using the single-tag method.

6. Lineshape analysis

The measured Born cross-section lineshape of $e^+e^- \rightarrow \Sigma^0 \bar{\Sigma}^0$ from $\sqrt{s} = 2.3864$ to 3.0200 GeV is shown in Fig. 3 (a). The cross sections measured in this analysis are in good agreement with that of BaBar, but with improved precision of at least 10% at low \sqrt{s} and over 50% above 2.5000 GeV as depicted in Fig. 3 (a). A perturbative QCD-motivated energy power function [46], given by

$$\sigma^B(s) = \frac{\beta C}{s} \left(1 + \frac{2m_B^2}{s}\right) \frac{c_0}{(s - c_1)^4 (\pi^2 + \ln^2(s/\Lambda_{\text{QCD}}^2))^2}, \quad (5)$$

is used to fit the lineshape, which has been successfully applied in the study of the $e^+e^- \rightarrow \Sigma^\pm \bar{\Sigma}^\mp$ reaction [16]. The free parameters in the fit are the normalization constants c_0 and c_1 , which describes the average effect of a set of possible intermediate states representing the form factors in the framework of the vector-meson-dominance model [47]. The QCD scale Λ_{QCD} is fixed to 0.3 GeV. In the fit, both statistical and systematic uncertainties are taken into account. The fit result is shown in Fig. 3 (a) with a fit quality of $\chi^2/\text{ndof} = 9.98/5$, where ndof is the number of degrees of freedom. To obtain a better understanding of the full set of Σ isospin states, the effective FFs of Σ^0 are compared with previous measurements of Σ^\pm at BESIII [16] as shown in Fig. 3 (b). An asymmetry in results is observed for the Σ isospin triplet, with the Σ^+ results lying above the Σ^0 results which in turn are higher than the Σ^- results. This behavior confirms the hypothesis that the effective FF is proportional to $\sum_q Q_q^2$ with $q = u, d, s$ quarks. Moreover, the effective form factor of the Σ^0 is compared with that of the Λ baryon to test the diquark correlation model. Our measurements are inconsistent with the hyperon-antihyperon ($Y\bar{Y}$) potential models from Ref. [13], where the cross section of $e^+e^- \rightarrow \Sigma^0 \bar{\Sigma}^0$ exhibits a weaker energy dependence than the pQCD power-law function in Eq. (5). We notice that there is a prediction for the non-resonant cross section of $e^+e^- \rightarrow \Sigma^0 \bar{\Sigma}^0$ at the

Table 3

The numerical results of Born cross sections σ^B and effective FFs $|G_{\text{eff}}|$ at each c.m. energy and the quantities used in the calculation, $(1 + \delta) = (1 + \delta') \frac{1}{|1 - \Pi|^2}$, defined in the text. The vacuum polarization factor $\frac{1}{|1 - \Pi|^2}$ is 1.04 from 2.3864 to 2.6464 GeV and 1.03 for the last two energy points. The energy point 2.9884 GeV is the luminosity-weighted combined dataset of the 2.9500, 2.9810, 3.0000 and 3.0200 GeV subsamples. The last column shows the statistical significance of the signal $S(\sigma)$ at each energy point. The values in parentheses represent the corresponding upper limit at the 90% confidence level. The first uncertainty is statistical, and the second is systematic.

\sqrt{s} (GeV)	\mathcal{L} (pb $^{-1}$)	ε (%)	$1 + \delta$	$N_{\text{obs}}(N_{\text{U.L.}})$	σ^B (pb)	$ G_{\text{eff}} $ ($\times 10^{-2}$)	$S(\sigma)$
2.3864	22.55	11.1	0.65	11.7 ± 5.8 (< 28.0)	$17.6 \pm 8.73 \pm 1.58$ (< 42.4)	$15.3 \pm 3.79 \pm 0.69$ (< 23.7)	2.3
2.3960	66.87	7.7	0.75	45.1 ± 11.2	$28.6 \pm 7.10 \pm 3.26$	$11.5 \pm 1.43 \pm 0.66$	4.5
2.5000	1.10	32.3	0.94	12.7 ± 6.4	$59.6 \pm 30.3 \pm 7.15$	$9.90 \pm 2.52 \pm 0.60$	3.1
2.6444	33.72	47.1	1.10	221 ± 25	$19.8 \pm 2.23 \pm 1.21$	$5.12 \pm 0.29 \pm 0.16$	12.4
2.6464	34.00	46.4	1.10	195 ± 24	$17.6 \pm 2.13 \pm 1.20$	$4.83 \pm 0.29 \pm 0.16$	11.9
2.9000	105.23	40.2	1.44	116 ± 17	$2.98 \pm 0.45 \pm 0.22$	$1.95 \pm 0.15 \pm 0.07$	9.4
2.9884	65.18	34.9	1.62	78.7 ± 13.9	$3.34 \pm 0.59 \pm 0.20$	$2.08 \pm 0.18 \pm 0.06$	9.0

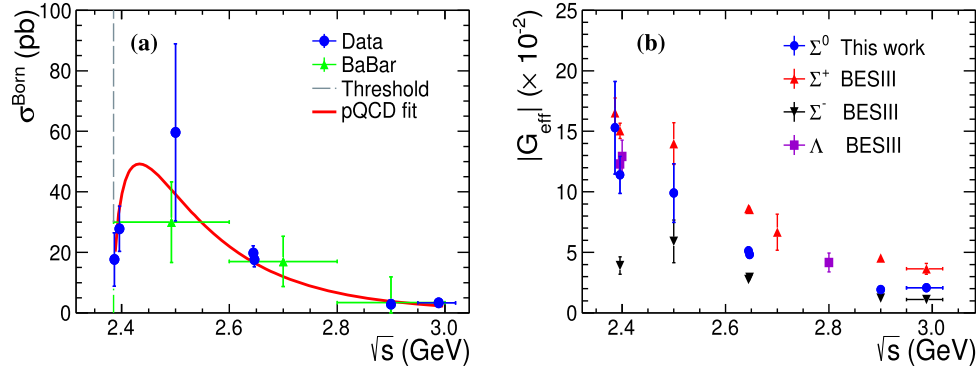


Fig. 3. (a) Comparison of the cross sections for $e^+e^- \rightarrow \Sigma^0 \bar{\Sigma}^0$ is represented by the dots with error bars in blue from this analysis, while triangles in green are results from BaBar [19]. It is noted that BaBar results do not include corrections for leptonic and hadronic vacuum polarization in the photon propagator. The solid line in red represents the fit with the pQCD energy power function. (b) Comparison of the effective FFs among this work and previous work of BESIII [12,16]. The blue circles represent the results from this analysis. The red upper triangles, black lower triangles and violet squares are from previous BESIII work.

J/ψ mass [48], based on an effective Lagrangian density, that is consistent with our result when extrapolated to $\sqrt{s} = 3.097$ GeV using Eq. (5).

7. Summary

In summary, data samples collected with the BESIII detector at c.m. energies between 2.3864 GeV and 3.0200 GeV have been exploited to perform measurements of the process $e^+e^- \rightarrow \Sigma^0 \bar{\Sigma}^0$. Born cross sections and effective FFs have been determined with a novel method for c.m. energies near production threshold at $\sqrt{s} = 2.3864$ and 2.3960 GeV. No significant signal is observed at $\sqrt{s} = 2.3864$ GeV and an upper limit on the cross section at the 90% C.L. is determined. No significant threshold effect is observed for this process, in common with the behavior seen in an earlier analysis of $e^+e^- \rightarrow \Sigma^\pm \bar{\Sigma}^\mp$ [16]. In addition, a single-tag method has been applied at c.m. energies between 2.3960 GeV and 3.0200 GeV. The measured results are in good agreement with previous results from BaBar [19], but the precision is significantly improved. The cross-section lineshape for $e^+e^- \rightarrow \Sigma^0 \bar{\Sigma}^0$ is well described by a pQCD-motivated function. An asymmetry of the effective FFs of Σ isospin triplet is observed, which is consistent with their incoherent sum of squared charges of valence quarks [16]. Our results also provide experimental inputs to test various theoretical models, such as $Y\bar{Y}$ potential [13] and diquark correlation [18] models.

Declaration of competing interest

The authors declare that they have no known competing financial interests or personal relationships that could have appeared to influence the work reported in this paper.

Acknowledgements

The BESIII collaboration thanks the staff of BEPCII and the IHEP computing center and the supercomputing center of USTC for their strong support. This work is supported in part by National Key Basic Research Program of China under Contract Nos. 2020YFA0406400, 2020YFA0406300; National Natural Science Foundation of China (NSFC) under Contracts Nos. 11625523, 11635010, 11735014, 11822506, 11835012, 11935015, 11935016, 11935018, 11950410506, 12061131003, 11961141012, 12035013, 11475169, 12122509, 12105276, 11335008, 11375170, 11475164, 11911530140, 11605196, 11605198, 11705192; the Chinese Academy of Sciences (CAS) Large-Scale Scientific Facility Program; Joint Large-Scale Scientific Facility Funds of the NSFC and CAS under Contracts Nos. U1732263, U1832207, U1532102, U1732263, U1832103, U2032111; CAS Key Research Program of Frontier Sciences under Contracts Nos. QYZDJ-SSW-SLH003, QYZDJ-SSW-SLH040; 100 Talents Program of CAS; INPAC and Shanghai Key Laboratory for Particle Physics and Cosmology; ERC under Contract No. 758462; German Research Foundation DFG under Contracts Nos. 443159800, Collaborative Research Center CRC 1044, FOR 2359; Istituto Nazionale di Fisica Nucleare, Italy; Ministry of Development of Turkey under Contract No. DPT2006K-120470; National Science and Technology fund; STFC (United Kingdom); The Knut and Alice Wallenberg Foundation (Sweden) under Contract No. 2016.0157; The Royal Society, UK under Contracts Nos. DH140054, DH160214; The Swedish Research Council; Olle Engkvist Foundation under Contract No. 200-0605; U.S. Department of Energy under Contracts Nos. DE-FG02-05ER41374, DE-SC-0012069.

References

- [1] R. Hofstadter, *Rev. Mod. Phys.* 28 (1956) 214.
- [2] L.S. Geng, J. Martin Camalich, L. Alvarez-Ruso, M.J. Vicente Vacas, *Phys. Rev. Lett.* 101 (2008) 222002.
- [3] S.J. Brodsky, G.R. Farrar, *Phys. Rev. D* 11 (1975) 1309.
- [4] J.R. Green, J.W. Negele, A.V. Pochinsky, S.N. Syritsyn, M. Engelhardt, S. Krieg, *Phys. Rev. D* 90 (2014) 074507.
- [5] G. Ramalho, K. Tsushima, A.W. Thomas, *J. Phys. G* 40 (2013) 015102; F. Gross, G. Ramalho, K. Tsushima, *Phys. Lett. B* 690 (2010) 183.
- [6] G. Eichmann, H. Sanchis-Alepuz, R. Williams, R. Alkofer, C.S. Fischer, *Prog. Part. Nucl. Phys.* 91 (2016) 1.
- [7] M. Ablikim, et al., BESIII Collaboration, *Chin. Phys. C* 44 (2020) 040001.
- [8] J.P. Lees, et al., BaBar Collaboration, *Phys. Rev. D* 87 (2013) 092005.
- [9] R.R. Akhmetshin, et al., CMD-3 Collaboration, *Phys. Lett. B* 759 (2016) 634.
- [10] M. Ablikim, et al., BESIII Collaboration, *Phys. Rev. Lett.* 120 (2018) 132001.
- [11] M.N. Achasov, et al., *Phys. Rev. D* 90 (2014) 112007.
- [12] M. Ablikim, et al., BESIII Collaboration, *Phys. Rev. D* 97 (2018) 032013; M. Ablikim, et al., BESIII Collaboration, *Phys. Rev. Lett.* 123 (2019) 122003.
- [13] J. Haidenbauer, U.-G. Meißner, L.-Y. Dai, *Phys. Rev. D* 103 (2021) 014028.
- [14] B. El-Bennich, M. Lacombe, B. Loiseau, S. Wycech, *Phys. Rev. C* 79 (2009) 054001.
- [15] R. Baldini Ferroli, S. Pacetti, A. Zallo, A. Zichichi, *Eur. Phys. J. A* 39 (2009) 315; R. Baldini Ferroli, S. Pacetti, A. Zallo, *Eur. Phys. J. A* 48 (2012) 33.
- [16] M. Ablikim, et al., BESIII Collaboration, *Phys. Lett. B* 814 (2021) 136110.
- [17] M. Ablikim, et al., BESIII Collaboration, *Phys. Rev. D* 103 (2021) 012005; M. Ablikim, et al., BESIII Collaboration, *Phys. Lett. B* 820 (2021) 136557.
- [18] M. Anselmino, et al., *Rev. Mod. Phys.* 65 (1993) 1199; R.L. Jaffe, F. Wilczek, *Phys. Rev. Lett.* 91 (2003) 232003; R.L. Jaffe, *Phys. Rep.* 409 (2005) 1.
- [19] B. Aubert, et al., BaBar Collaboration, *Phys. Rev. D* 76 (2007) 092006.
- [20] M. Ablikim, et al., BESIII Collaboration, *Chin. Phys. C* 41 (2017) 063001.
- [21] M. Ablikim, et al., BESIII Collaboration, *Nucl. Instrum. Methods A* 614 (2010) 345.
- [22] S. Agostinelli, et al., GEANT4 Collaboration, *Nucl. Instrum. Methods A* 506 (2003) 250.
- [23] R.G. Ping, *Chin. Phys. C* 38 (2014) 083001.
- [24] P. Elisabetta, F. Göran, K. Andrzej, L. Stefan, S. Jiao Jiao, *Phys. Rev. D* 99 (2019) 056008; F. Göran, S. Karin, *Phys. Rev. D* 101 (2020) 033002.
- [25] D.J. Lange, *Nucl. Instrum. Methods A* 462 (2001) 152; R.G. Ping, et al., *Chin. Phys. C* 32 (2008) 599.
- [26] Due to the poor determination or unknown ratio of $|G_E/G_M|$ and relative phase ($\Delta\Phi$) between the G_E and G_M FFs experimentally, we set the value of α corresponding to $G_E = G_M$ assumption and $\Delta\Phi = 45^\circ$.
- [27] P.A. Zyla, et al., Particle Data Group, *Prog. Theor. Exp. Phys.* 2020 (2020) 083C01.
- [28] B. Andersson, H. Hu, arXiv:hep-ph/9910285.
- [29] E. Richter-Was, *Phys. Lett. B* 303 (1993) 163.
- [30] G. Balossini, et al., *Nucl. Phys. B* 758 (2006) 227; G. Balossini, et al., *Phys. Lett. B* 663 (2008) 209.
- [31] S. Nova, A. Olchevski, T. Todorov, DELPHI-90-35 PROG 152, 1990; S. Nova, A. Olchevski, T. Todorov, DELPHI Collaboration, DELPHI 90-35 PROG 152, 1990.
- [32] N. Cabibbo, R. Gatto, *Phys. Rev. Lett.* 4 (1960) 313; *Phys. Rev.* 124 (1961) 1577.
- [33] J. Schwinger, *Particle, Sources, and Field*, vol. 3, Perseus Books Publishing, Massachusetts, 1998.
- [34] A.B. Arbuzov, T.V. Kopylova, *J. High Energy Phys.* 1204 (2012) 009.
- [35] B. Aubert, et al., BaBar Collaboration, *Phys. Rev. D* 76 (2007) 092006.
- [36] S. Actis, et al., Working Group on Radiative Corrections and Monte Carlo Generators for Low Energies, *Eur. Phys. J. C* 66 (2010) 585.
- [37] W. Sun, T. Liu, M. Jing, et al., *Front. Phys.* 16 (2021) 64501.
- [38] X.Y. Zhou, S.X. Du, G. Li, C.P. Shen, *Comput. Phys. Commun.* 258 (2021) 107540.
- [39] K. Stenson, arXiv:physics/0605236; J. Lundberg, J. Conrad, W. Rolke, A. Lopez, *Comput. Phys. Commun.* 181 (2010) 683.
- [40] S.S. Wilks, The large-sample distribution of the likelihood ration for testing composite hypotheses, *Ann. Math. Stat.* 9 (1938) 60–62.
- [41] R. Wanke, *Data Analysis in High Energy Physics*, Wiley-VCH Verlag GmbH and Co. KGaA, Singapore, 2013, pp. 263–280.
- [42] M. Ablikim, et al., BESIII Collaboration, *Phys. Rev. D* 101 (2020) 092002.
- [43] E.V. Abakumova, et al., *Nucl. Instrum. Methods A* 659 (2011) 21.
- [44] M. Xu, et al., *Chin. Phys. C* 33 (2009) 428.
- [45] M. Ablikim, et al., BESIII Collaboration, *Phys. Rev. D* 92 (2015) 052003.
- [46] S. Pacetti, R. Baldini Ferroli, E. Tomasi Gustafsson, *Phys. Rep.* 550–551 (2015) 1.
- [47] H.W. Hammer, U.G. Meißner, D. Drechsel, *Phys. Lett. B* 385 (1996) 343.
- [48] R. Baldini Ferroli, A. Mangoni, S. Pacetti, K. Zhu, *Phys. Lett. B* 799 (2019) 135041.